

## MELTING MODE THRESHOLDS IN LASER POWDER BED FUSION AND THEIR APPLICATION TOWARDS PROCESS PARAMETER DEVELOPMENT

S. Patel\*, M. L. Vlasea\*

\*Department of Mechanical and Mechatronics Engineering, University of Waterloo, Waterloo, ON N2L 3G1

### Abstract

Depending on processing conditions, laser powder bed fusion (LPBF) has broadly two different processing regimes, conduction and keyhole mode. Heat conduction governs the melt pool morphology observed in conduction mode melting. In contrast, keyhole mode melting is observed when the morphology of the molten pool is controlled by thermo-capillary convection and recoil momentum pressure generated by vaporization of a given material. Additionally, there exists another melting mode called transition mode wherein the dominance of conduction or convection depends on processing conditions. In this work, we use an analytical temperature prediction model, along with normalized processing diagrams, to obtain a processing window for achieving high-density three-dimensional Ti-6Al-4V parts on a continuous beam exposure LPBF system. The normalized processing diagrams in this work help visualize the three melting modes - conduction, transition, and keyhole mode. The temperature prediction model can be used to predict the thresholds between the three melting modes. This work can be used for understanding the physical origins of defects in three-dimensional LPBF parts, as well as lower the risk of costly experimentation to go from powder to near fully dense products.

### Introduction

The LPBF process is affected by more than 130 processing parameters [1]. There are emerging research efforts in understanding the scale of impact each parameter has and how different parameters are correlated. To be able to produce consistent LPBF parts, these effects and dependencies need to be better understood.

LPBF involves heating, melting, and solidification of a material by a moving laser in a layer by layer manner. Due to the locally concentrated energy input, localized thermal cycles are generated, leading to residual stresses. This is particularly prevalent in LPBF of titanium alloys. Residual stresses can result in deformation, cracking, and change in mechanical strength [2,3]. Additionally, literature [4] has shown that the tensile properties of titanium alloys processed by LPBF are influenced not only by intrinsic microstructure but are also influenced by defect characteristics such as pore size, shape, orientation, and location. The research proposed in this document is focused on developing a better understanding of the phenomena occurring at the mesoscale in LPBF. Mesoscale phenomena involve the study of porosity due to insufficient melting or excessive melting in conduction, transition and keyhole mode LPBF. To understand the phenomena occurring at the mesoscale of LPBF, it is important to develop temperature prediction models which forecast melt pool morphology and heat transfer mechanism changes, from a dominance of conductive heat transfer to a dominance of convective heat transfer. These temperature prediction models can also be used to predict the material behaviour during melting, solidification, and re-melting cycles, which have a direct impact on microstructure and thereby, on mechanical properties.

In LPBF, achieving near fully-dense parts is one of the most important criteria for practical applications [5]. In our previous work, we have proposed an enhanced heat conduction-based temperature prediction model to predict the threshold between conduction, transition and keyhole modes tailored for LPBF [6]. This temperature prediction model, in conjunction with normalized processing diagrams, enable the mapping and prediction of the three melting modes for continuous and modulated LPBF systems, independent of powder layer thickness. This approach allows us to obtain processing diagrams for a given LPBF system and material, thereby reducing the need for costly experimentation to identify the optimal processing windows for obtaining near fully dense parts. In this work, we present results of our approach to identify the optimal processing window for Ti-6Al-4V using an EOS M290 LPBF system.

## Methods

### *Construction of Normalized Processing Diagrams with Melting Mode Thresholds*

To obtain the normalized processing diagram of Ti-6Al-4V, the equation derivations from earlier work was followed [6] to define the a dimensionless heat input term,  $E^*$ , as:

$$E^* = \frac{q^*}{l^*} = \frac{AP}{2\lambda l_i(T_m - T_0)} \quad (1)$$

In equation (1),  $q^*$  is dimensionless beam power and  $l^*$  is dimensionless layer thickness [7,8]. Furthermore,  $A$  is the laser absorptivity,  $P$  is the laser power [W],  $\lambda$  is the thermal conductivity [W/(m.K)],  $T_m$  is the melting temperature [K], and  $T_0$  is the initial (or powder bed) temperature [K]. The dimensionless beam velocity term,  $v^*$ , is defined as [7]:

$$v^* = \frac{vr_B}{\alpha} \quad (2)$$

In equation (2),  $v$  is the laser beam velocity [m/s],  $r_B$  is the beam spot radius [m], and  $\alpha$  is the thermal diffusivity [m<sup>2</sup>/s]. Values for material constants are taken at the solidus temperature for a given material from ref. [9] & [10]. In this work, the values of laser absorptivity,  $A$ , are noted as being dependent on melting mode and beam spot size as summarized in our prior work [6], which has been observed through micro-calorimetry approaches for LPBF [11–13]. The dimensionless beam power term,  $q^*$ , and the dimensionless layer thickness term,  $l^*$ , are defined in equations (3) and (4) respectively [7,8].

$$q^* = \frac{AP}{r_B\lambda(T_m - T_0)} \quad (3)$$

$$l^* = \frac{2 \cdot l_i}{r_B} \quad (4)$$

In equation (4),  $l_i$  is the powder layer thickness [m]. The analytical temperature prediction model used to predict melting mode thresholds involves obtaining the dimensionless peak temperatures,  $T_p^*$ , in the melt pool given by:

$$T_p^* = \frac{3}{2\sqrt{2\pi}e^{0.75}} \cdot \frac{E^*}{v^*} \cdot \frac{1}{(z^* + z_0^*)^2} \quad (5)$$

The detailed derivation for equation (5) is given in our previous work [6]. This model is an enhancement of the work by Ashby and Easterling [14] tailored for LPBF. In equation (5),  $z^*$  is dimensionless depth (equation (7)), and  $z_0^*$  is the dimensionless distance of the apparent source above the surface of the melt pool (equation (8)). The dimensionless peak temperature term is defined in equation (6).

$$T_p^* = \frac{T_p - T_0}{T_m - T_0} \quad (6)$$

$$z^* = \frac{z}{r_B} \quad (7)$$

$$z_0^* = \frac{z_0}{r_B} \quad (8)$$

The term  $z_0^*$  is obtained by equating  $T_p^*$  from equation (5) to a solution for peak surface temperature produced by a stationary beam acting for a time equal to the beam interaction time ( $t_B = 2 \cdot r_B / v$ ) [15]. The detailed derivation for obtaining  $z_0^*$  is given in [6]; the solution for the term  $z_0^*$  is given below in equation (9).

$$z_0^* = \sqrt{\frac{3\sqrt{\pi}}{2\sqrt{2}e^{0.75}} \cdot \frac{1}{v^* \tan^{-1}(\sqrt{8/v^*})}} \quad (9)$$

For low reflectivity, low thermal conductivity, and high surface tension materials such as Ti-6Al-4V, SS 316L, and Inconel 625, the threshold between conduction mode and transition mode is predicted to be when the vaporization depth exceeds 0.5 times beam spot radius of a given LPBF system [6]. This corresponds to a front vaporization wall angle ( $\theta$ ) of  $75.96^\circ$ . The front vaporization wall angle,  $\theta$ , is obtained from the work of Fabbro et al. [16] and is given by:

$$\theta = \tan^{-1}\left(\frac{\sigma}{d_v}\right) \quad (10)$$

In equation (10),  $\sigma$  is the beam spot diameter ( $\sigma = 2 \cdot r_B$ ) [m], and  $d_v$  is the vaporization depth [m]. The threshold between transition mode and keyhole mode is predicted to be when the vaporization depth exceeds 0.8 times the beam spot radius of a given LPBF system. This corresponds to a front vaporization wall angle ( $\theta$ ) of  $68.2^\circ$  [6]. In the following section, we describe the methodology used to obtain near fully dense Ti-6Al-4V parts on an EOS M290 LPBF system along with application of the melting mode thresholds model towards understanding the physical origin of defects via non-destructive testing (X-ray computed tomography scans).

### ***Experimental Methods for Process Window Identification***

An experimental plan is defined for manufacturing three-dimensional Ti-6Al-4V parts on a continuous LPBF (EOS M290, beam spot radius at focal point,  $r_B = 40\mu m$ ). To define the experimental plan, it is first assumed that all of the experimental design points to lie in the transition mode, and hence use a laser absorptivity value of 0.605 obtained from prior work[6]. Subsequently, the processing parameters (laser power and laser beam velocity) are chosen such that the experiment is able to approximately span the conduction, transition, and keyhole modes as shown in the initial LPBF diagram in Figure 1 (A). The green line corresponds to the threshold between conduction and transition mode, whereas the blue line corresponds the threshold between transition and keyhole mode.  $T_p^* = 1.72$  corresponds to the vaporization temperature of Ti-6Al-4V and  $z^* = 0.5$  thereby corresponds to a vaporization depth of 0.5 times the beam spot radius of EOS M290 used in this work ( $r_B = 40\mu m$ ). Similarly,  $z^* = 0.8$  corresponds to a vaporization depth of 0.8 times the beam spot radius used in this work. Sample 1 was designed to fall in conduction mode and sample 4 is touching the keyhole mode threshold; the absorptivity coefficients for the two samples is then adjusted to 0.41 and 0.8 respectively as per [6], to better match the physics of the corresponding melting mode. The final processing diagram is obtained as shown in Figure 1 (B).

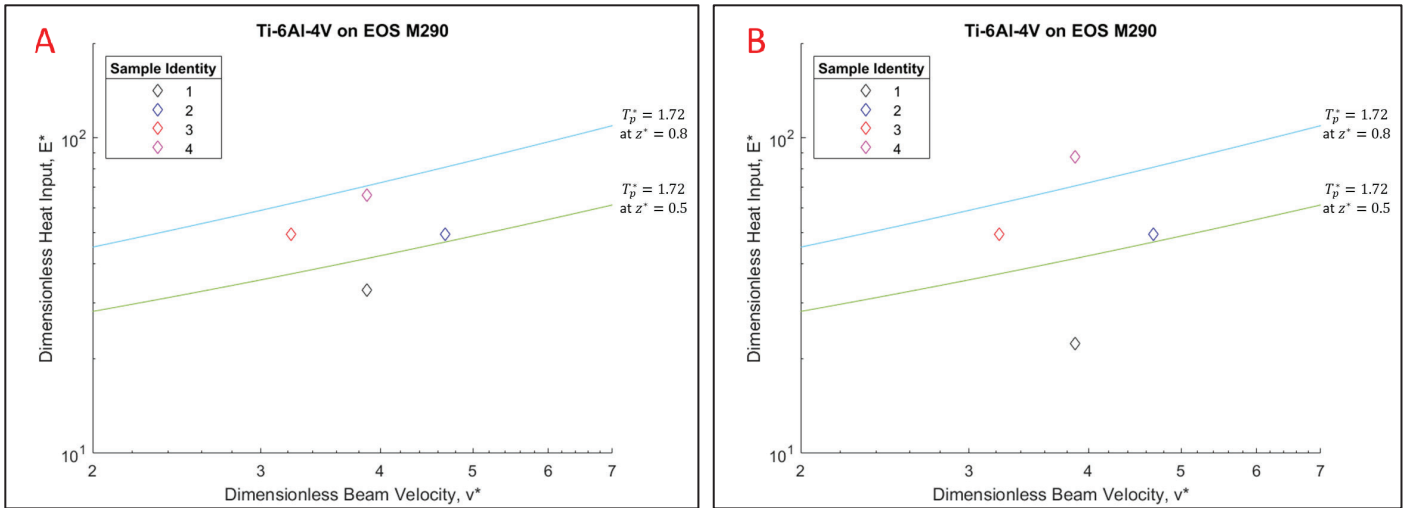


**Figure 1. Initial estimate (A) and final (B) processing diagram for the four samples manufactured on EOS M290, a continuous LPBF system; and model predictions of the onset of transition mode and keyhole mode.**

The samples manufactured were cylinders of diameter 5 mm, and height 8 mm. These samples were built on top of support structures (5 mm in height) as illustrated in Figure 2 (A). The support structures are manufactured at a power of 100 W and a velocity of 750 mm/s (which lies in conduction mode). The build plate layout of the parts with respect to the gas flow and powder flow is shown in Figure 2 (B).

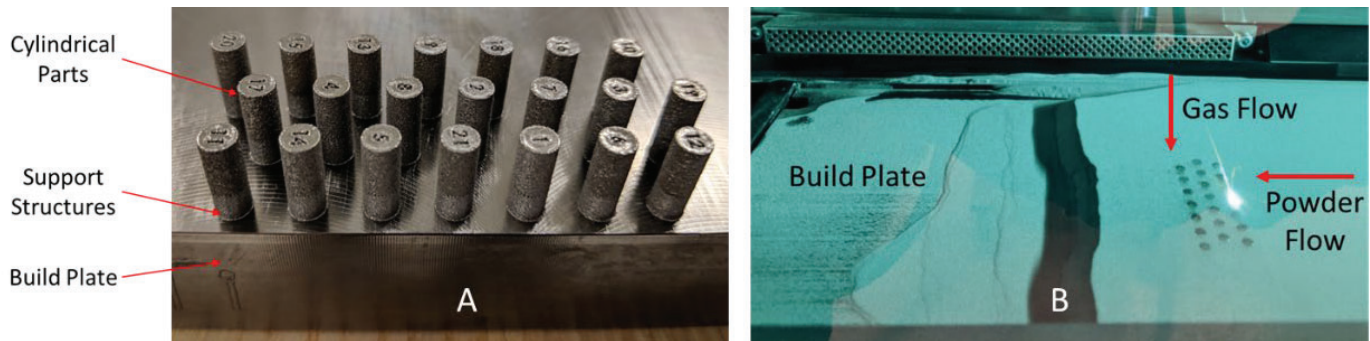


**Figure 2. Illustration showing the manufactured cylinders along with support structures on the build plate of EOS M290 (A), layout for the manufactured cylinders showing the argon gas flow and powder flow direction (B).**

The primary processing parameters for the core of the four samples from Figure 1 are summarized in Table 1. Within each layer, the scan path follows this order: scanning of the core using the meander scanning strategy, followed by a border scan (power – 100 W; velocity – 980 mm/s); all border scans being kept constant in parameters. The meander scanning strategy involves scanning using straight line vector path from each side of the border.

**Table 1. Primary processing parameters for the four samples manufactured on EOS M290.**

Sample Identity	Core Parameters				Melting Mode
	Power, $P$ [W]	Velocity, $v$ [mm/s]	Powder Layer thickness, $l_t$ [ $\mu\text{m}$ ]	Hatch Distance, $h_d$ [ $\mu\text{m}$ ]	
1	150	1200	30	100	Conduction
2	225	1450			Transition
3	225	1000			Transition
4	300	1200			Keyhole

## *X-ray Computed Tomography Methods*

The manufactured cylinders were removed off the build plate and analyzed for porosity characteristics using a 3D X-ray computed tomography (CT) scanner (ZEISS Xradia 520 Versa) using a 7  $\mu\text{m}$  voxel size. The processing parameters used to obtain the X-ray CT scanning results are shown in Table 2. To visualize the pore distribution within each sample, the CT scanned files were analyzed using an image processing software (Dragonfly 3.0, Object Research Systems Inc., Montreal, QC) [17]. The image data obtained from CT scanning was thresholded and binarized. To visualize the pore space, a minimum-intensity projection (MIP) method is employed. The MIP method is a projection of the pore space onto one single image plane, and it serves as a good indication of the persistence and general location of the pores.

*Table 2. X-ray computed tomography parameters used for scanning the four Ti-6Al-4V cylindrical parts*

<b>Parameter</b>	<b>Unit</b>	<b>Value</b>
Voxel size	[ $\mu\text{m}$ ]	7
Source power	[W]	10
X-ray energy	[kV]	140
Filter	-	Air
X-ray optic	-	0.4 $\times$ lens
Source position	[mm]	13.53
Detector position	[mm]	11.90
Exposure time	[s]	20.5
Number of projections	-	1201
Binning level	-	2

Due to interpolation defects from rotation, areas near the top and bottom of each manufactured cylinder tended to display CT beam hardening artifacts and were hence cropped from the analyzed region. Additionally, near the top and bottom of samples the presence of X-ray-related cone angle defects affected the visual clarity of the images and were hence also cropped out. In total, approximately 20% of a given sample's height (about 1.6 mm) was not included in this analysis to avoid uncertainty introduced by CT beam effects.

## **Results and Discussion**

The minimum intensity projection (MIP) images of the four representative samples are shown in Figure 3, capturing the defect space from the entire region of interest, flattened onto the XY plane. The solid part is represented by the white colored regions, and the defects in a given part are given by the black colored regions in Figure 3. As we can observe from Figure 3 and Figure 4, sample 1 (which is in conduction mode) has a concentration of mostly irregularly shaped defects when compared to sample 4 (which is in keyhole mode) which has a combination of irregularly shaped defects as well as nearly spherical defects.

The porosity in sample 1 can be attributed to lack of fusion defects, beam path trajectory stitching, and/or random defects expected with conduction mode melt pools [18,19]. Lack of fusion defects are commonly observed when the heat input is considerably lower than the transition mode threshold as reported by King et al. [20]. Since the density of the sample is 99.982%, it implies that most of the melt pools created were such that their morphology did not lead directly to lack of fusion defects. Recent research from our research group [21,22] along with high-speed imaging studies on ejecta [23] have shown that ejecta (particles with a size much larger than the mean particle size of the feedstock powder used) have a direct impact on melt pool geometry and hence could be a potential cause for the defects that we observe in this melting mode. In addition, powder denudation effects [24,25] alter the melt pool morphology as well which could lead to melt pools with insufficient depth and/or width thereby causing inadequate stitching of melt pools needed to obtain fully-dense LPBF parts. In this experiment, the higher beam velocities and lower power used for sample 1 could also lead to surface tension-driven breaking of the melt tracks, which lead to undesirable balling effects due to a variant of

the Plateau-Rayleigh instability theory [26,27]. These irregular surfaces can then affect powder spreading in the following layers thereby impact the stability of melt pools due to inhomogeneous powder and solid metal distribution. The aspect ratio of pores observed in this melting mode is typically indicative of irregular-shaped defects, with a low aspect ratio [28]. This same effect was observed in this experiment, as visualized in Figure 4.

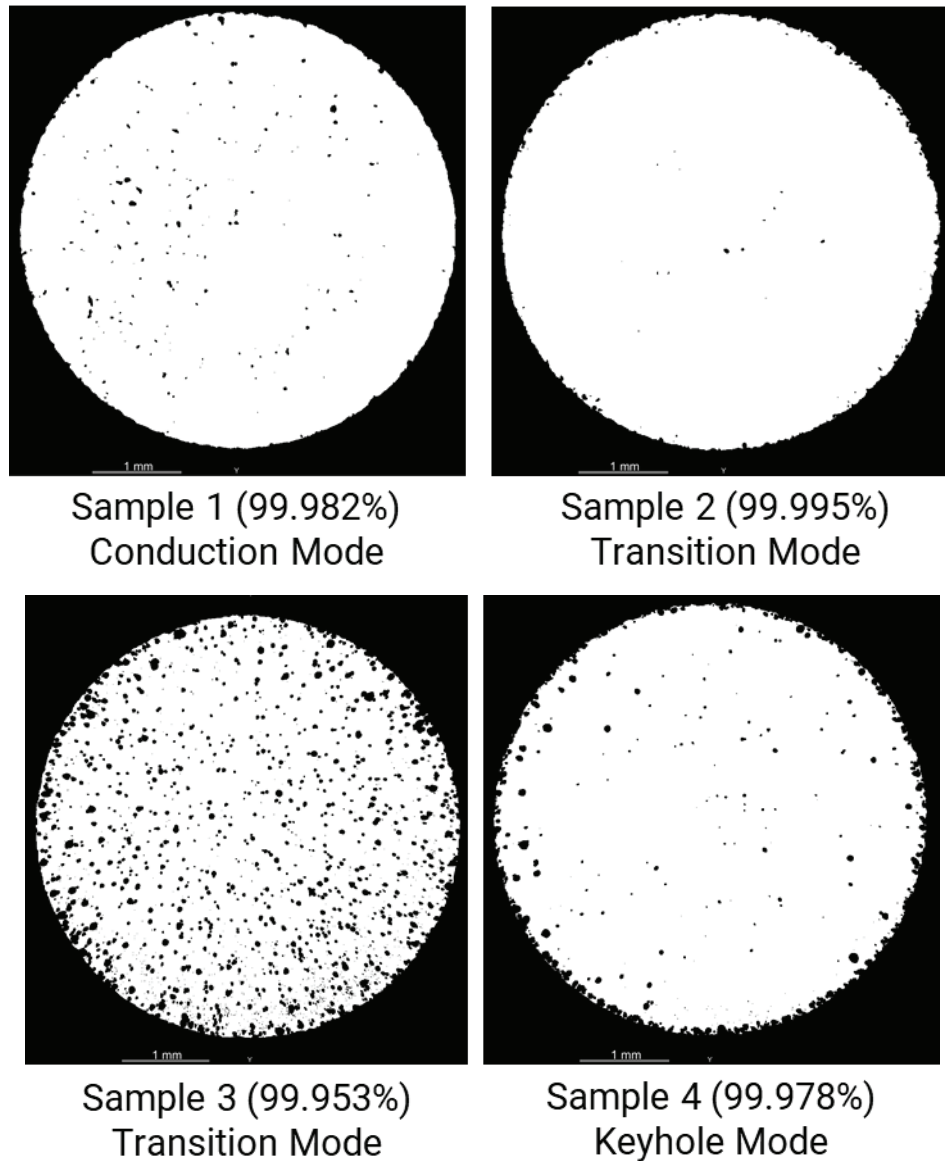
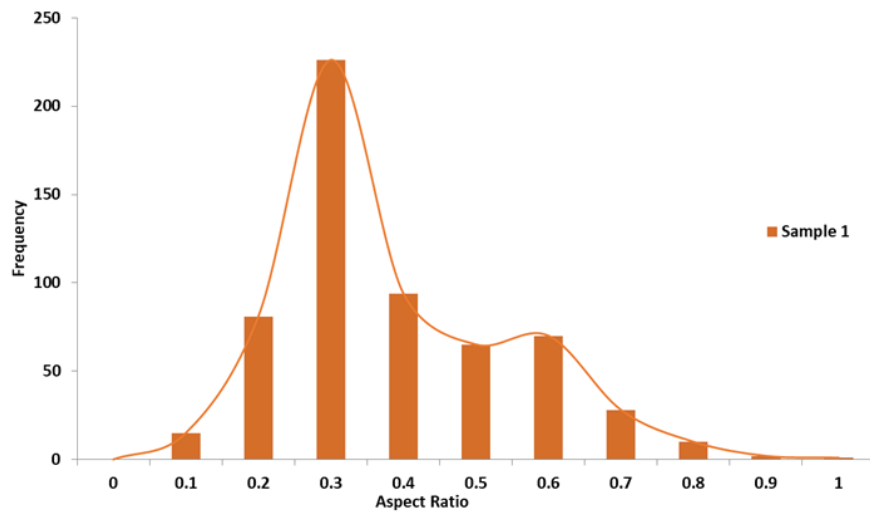


**Figure 3. Minimum intensity projection of the pore space along with build direction of the samples 1-4 from EOS M290 onto a single plane. Density of each sample is given in the brackets.**

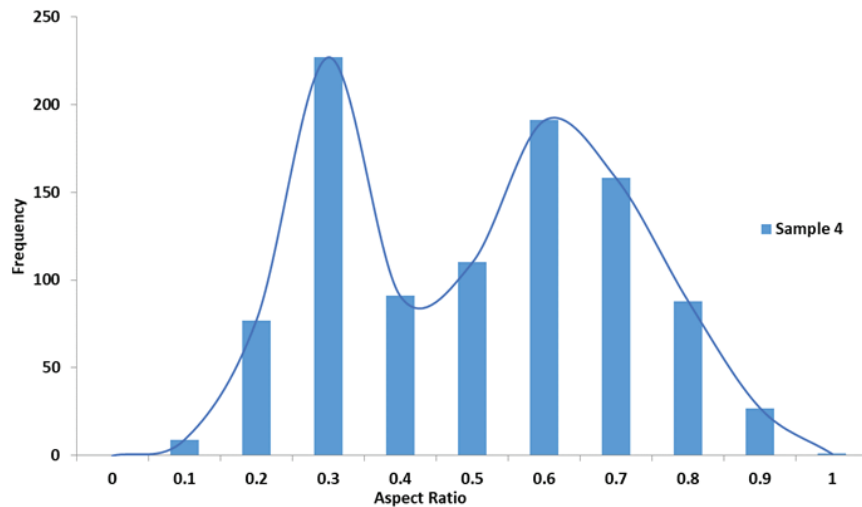
When the predicted melting mode is keyhole mode (sample 4), there is a prevalence of more spherical defects, as proven by the higher number of high aspect ratio defects shown in Figure 4; this is expected for melt pools in keyhole mode [20]. If thermo-capillary flow, referred to as Marangoni flow induced by surface temperature gradients, also known as Bénard–Marangoni flow, and recoil (vapour) pressure due to material vaporization are not balanced out, melt pool instabilities occur [29]. Such instabilities are known to create defects during keyhole mode LPBF [30].

Keyhole mode defects could occur due to a multitude of reasons, as discussed by Kaplan in [31]. The mechanisms for defect formation in keyhole mode include collapse and rapid irregular solidification of the bottom section of the vaporized region (irregularly shaped defects), the cavities from the bottom section of the vaporized region which contract to a spherical bubble and solidify as a pore (spherical defects), pores created by

the vapour jet of the vaporized metal (spherical defects), and pore coalescence (spherical and irregularly shaped defects) [31]. Another mechanism for irregular-shaped defect formation in keyhole mode processing of titanium alloys at high laser beam velocities (samples 2 and 4) could be the elongated molten pool regions near the side and rear walls of the vaporized region, which rise from the top of the melt pool thereby breaking into droplets of molten metal called melt pool splatter [32]. Powder ejecta [23] is also expected cause irregularities on the layer being printed and could thereby be an additional cause of irregular-shaped defects in this melting mode. The high momentum flow along the vaporized region that causes powder denudation also mixes in voids that exist between powder particles in the region along the melt pool length that lies between the vaporized portion direction underneath the laser beam and the tail end of a given melt pool. A partially melted particle in the transition region that does not completely merge with the melt pool increase the surface roughness of a given layer and thereby deteriorate the wetting behaviour of the following layer causing additional melt pool instabilities possibly leading to defect formation [33,34]. These mechanisms of defect formation in keyhole mode melt pools explain the presence of both spherical and irregularly shaped defect in the keyhole mode part (sample 4) as observed in Figure 4.



Sample 1 - Conduction Mode



Sample 4 - Keyhole Mode

**Figure 4. Aspect ratio comparison of the defects in the conduction mode (sample 1) and keyhole mode (sample 2) Ti-6Al-4V parts manufactured on the EOS M290 LPBF system.**

One thing to note is that the amount of large melt pool splatters observed were higher in low velocity regimes for keyhole laser welding of titanium when compared to higher velocities [32]. These larger melt pool splatters would be expected to cause greater irregularities in the layer being printed and thereby affect powder spreading in the following layers leading to additional causes for instabilities in the melt pool. This could be one of the potential reasons for the lowest density observed in sample 3. However, laser welding beam spot sizes (280  $\mu\text{m}$  in [32]) are considerably higher than LPBF beam spot sizes (80  $\mu\text{m}$  in the current work) and this could lead to differences in melt pool spatter behaviour which need to be further explored.

Sample 2, which lies in the transition melting mode, was observed to be the highest density sample in this present work. Since transition mode melt pools have a higher front vaporization wall angle ( $\theta$ ) compared to keyhole mode melt pools, the ratio of width of the vaporized region to the depth of the vaporized region is expected to be higher in transition mode due to the angle of incidence of the laser beam on the vaporized portion of the melt pools. This leads to larger area of a high temperature gradient region in transition mode melt pools. Hojjatzadeh et al. [35] have shown that larger areas of high temperature gradient regions lead to greater thermocapillary force. This thermocapillary force which can overcome the melt flow induced drag force in the laser interaction region drives pores to move in the direction of the temperature gradient and thereby escaping the melt pool. Since transition mode melt pools are expected to have larger areas of temperature gradients, more pores can escape melt pool before solidification when compared to keyhole mode melt pools. This could be a potential reason for the higher density observed in sample 2 (transition mode) when compared to sample 4 (keyhole mode).

It must be noted that for all the four samples, the origin of defects listed are not exhaustive by any means. There are multiple other factors such as powder feedstock characteristics, powder flow characteristics, build plate characteristics, laser beam characteristics, build file setup, and build chamber conditions which could directly or indirectly contribute towards defects in three-dimensional LPBF parts [6]. This study was intended to be a preliminary work in understanding how process diagrams and melting mode thresholds can be used to design experiments. Further work will focus on a deeper understanding of porosity in each melting mode through both exploring literature, modeling, and experimental datasets.

## **Conclusions**

Normalized processing diagrams, along with a temperature prediction model to predict melting mode thresholds, were used to drive an experimental design as a starting point in process parameter optimization, as well as to understand the physical origin of defects in three-dimensional Ti-6Al-4V parts manufactured on an EOS M290 LPBF system. In the conduction mode sample, majority of the defects observed were irregularly shaped, which may result from a combination of lack of fusion defects, beam path stitching defects, and random defects. In the keyhole mode sample, a mix of both spherical and irregularly shaped defects was observed which is due to the instability of melt pools as a result of excessive heat input. One of the transition mode samples had the lowest density which could be due to the increased amount of large melt pool spatter expected in low velocity transition and keyhole mode melting. Finally, the highest density part was also obtained in transition mode, albeit at a higher velocity setting. The processing parameters for this part could be such that the forces created of thermocapillary flow and vaporization of the melt pools are able to balance each other out leads to mostly stable melt pools. Further work will focus on a deeper understanding of porosity in each melting mode through both exploring literature, modeling, and experimental datasets.

## **Acknowledgments**

The authors appreciate the funding support received from Federal Economic Development Agency for Southern Ontario (FedDev Ontario, grant # 809104). In addition, the authors would like to acknowledge the help of Henry Ma, Jerry Ratthapakdee, and Karl Rautenberg in helping with the deployment and characterization of builds, and the motivation and support of the MSAM Group at University of Waterloo.

## References

- [1] I. Yadroitsev, Selective laser melting: Direct manufacturing of 3D-objects by selective laser melting of metal powders, LAP LAMBERT Academic Publishing, Saarbrücken, 2009.
- [2] P. Mercelis, J.-P. Kruth, Residual stresses in selective laser sintering and selective laser melting, *Rapid Prototyp. J.* 12 (2006) 254–265.
- [3] C. Li, Z.Y. Liu, X.Y. Fang, Y.B. Guo, Residual Stress in Metal Additive Manufacturing, *Procedia CIRP.* 71 (2018) 348–353. doi:10.1016/j.procir.2018.05.039.
- [4] T. Voisin, N.P. Calta, S.A. Khairallah, J.B. Forien, L. Balogh, R.W. Cunningham, A.D. Rollett, Y.M. Wang, Defects-dictated tensile properties of selective laser melted Ti-6Al-4V, *Mater. Des.* 158 (2018) 113–126. doi:10.1016/j.matdes.2018.08.004.
- [5] Y. (Morris) Wang, C. Kamath, T. Voisin, Z. Li, A processing diagram for high-density Ti-6Al-4V by selective laser melting, *Rapid Prototyp. J.* 24 (2018) 1469–1478. doi:10.1108/RPJ-11-2017-0228.
- [6] S. Patel, M. Vlasea, Melting modes in laser powder bed fusion (under review), (2019).
- [7] J.C. Ion, H.R. Shercliff, M.F. Ashby, Diagrams for laser materials processing, *Acta Metall. Mater.* 40 (1992) 1539–1551.
- [8] M. Thomas, G.J. Baxter, I. Todd, Normalised model-based processing diagrams for additive layer manufacture of engineering alloys, *Acta Mater.* 108 (2016) 26–35.
- [9] T. Mukherjee, H.L. Wei, A. De, T. DebRoy, Heat and fluid flow in additive manufacturing – Part II: Powder bed fusion of stainless steel, and titanium, nickel and aluminum base alloys, *Comput. Mater. Sci.* 150 (2018) 369–380. doi:10.1016/j.commatsci.2018.04.027.
- [10] K.C. Mills, Recommended Values of Thermophysical Properties for Selected Commercial Alloys, Woodhead Publishing, 2002.
- [11] J. Ye, S.A. Khairallah, A.M. Rubenchik, M.F. Crumb, G. Guss, J. Belak, M.J. Matthews, Energy Coupling Mechanisms and Scaling Behavior Associated with Laser Powder Bed Fusion Additive Manufacturing, *Adv. Eng. Mater.* 0 (n.d.) 1900185. doi:10.1002/adem.201900185.
- [12] J. Ye, A.M. Rubenchik, M.F. Crumb, G. Guss, M.J. Matthews, Laser Absorption and Scaling Behavior in Powder Bed Fusion Additive Manufacturing of Metals, in: *Conf. Lasers Electro-Opt. 2018 Pap. JW2A117*, Optical Society of America, 2018: p. JW2A.117. doi:10.1364/CLEO\_AT.2018.JW2A.117.
- [13] J. Trapp, A.M. Rubenchik, G. Guss, M.J. Matthews, In situ absorptivity measurements of metallic powders during laser powder-bed fusion additive manufacturing, *Appl. Mater. Today.* 9 (2017) 341–349. doi:10.1016/j.apmt.2017.08.006.
- [14] M.F. Ashby, K.E. Easterling, The transformation hardening of steel surfaces by laser beams—I. Hypoeutectoid steels, *Acta Metall.* 32 (1984) 1935–1948. doi:10.1016/0001-6160(84)90175-5.
- [15] J.F. Ready, Effects of High Power Laser Radiation, Academic Press, London, 1971.
- [16] R. Fabbro, K. Chouf, Keyhole modeling during laser welding, *J. Appl. Phys.* 87 (2000) 4075–4083. doi:10.1063/1.373033.
- [17] Dragonfly | 3D Visualization and Analysis Solutions for Scientific and Industrial Data | ORS, (n.d.). <https://www.theobjects.com/dragonfly/> (accessed August 25, 2019).
- [18] W.E. King, H.D. Barth, V.M. Castillo, G.F. Gallegos, J.W. Gibbs, D.E. Hahn, C. Kamath, A.M. Rubenchik, Observation of keyhole-mode laser melting in laser powder-bed fusion additive manufacturing, *J. Mater. Process. Technol.* 214 (2014) 2915–2925. doi:10.1016/j.jmatprotec.2014.06.005.
- [19] S.A. Khairallah, A.T. Anderson, A. Rubenchik, W.E. King, Laser powder-bed fusion additive manufacturing: Physics of complex melt flow and formation mechanisms of pores, spatter, and denudation zones, *Acta Mater.* 108 (2016) 36–45. doi:10.1016/j.actamat.2016.02.014.
- [20] W.E. King, H.D. Barth, V.M. Castillo, G.F. Gallegos, J.W. Gibbs, D.E. Hahn, C. Kamath, A.M. Rubenchik, Observation of keyhole-mode laser melting in laser powder-bed fusion additive manufacturing, *J. Mater. Process. Technol.* 214 (2014) 2915–2925. doi:10.1016/j.jmatprotec.2014.06.005.
- [21] R. Esmailizadeh, U. Ali, A. Keshavarzkermani, Y. Mahmoodkhani, E. Marzbanrad, E. Toyserkani, On the effect of spatter particles distribution on the quality of Hastelloy X parts made by laser powder-bed fusion additive manufacturing, *J. Manuf. Process.* 37 (2019) 11–20. doi:10.1016/j.jmapro.2018.11.012.
- [22] U. Ali, R. Esmailizadeh, F. Ahmed, D. Sarker, W. Muhammad, A. Keshavarzkermani, Y. Mahmoodkhani, E. Marzbanrad, E. Toyserkani, Identification and characterization of spatter particles and

- their effect on surface roughness, density and mechanical response of 17-4 PH stainless steel laser powder-bed fusion parts, *Mater. Sci. Eng. A*. 756 (2019) 98–107. doi:10.1016/j.msea.2019.04.026.
- [23] A.R. Nassar, M.A. Gundermann, E.W. Reutzel, P. Guerrier, M.H. Krane, M.J. Weldon, Formation processes for large ejecta and interactions with melt pool formation in powder bed fusion additive manufacturing, *Sci. Rep.* 9 (2019) 5038. doi:10.1038/s41598-019-41415-7.
- [24] M.J. Matthews, G. Guss, S.A. Khairallah, A.M. Rubenchik, P.J. Depond, W.E. King, Denudation of metal powder layers in laser powder bed fusion processes, *Acta Mater.* 114 (2016) 33–42. doi:10.1016/j.actamat.2016.05.017.
- [25] S.A. Khairallah, A.T. Anderson, A. Rubenchik, W.E. King, Laser powder-bed fusion additive manufacturing: Physics of complex melt flow and formation mechanisms of pores, spatter, and denudation zones, *Acta Mater.* 108 (2016) 36–45. doi:10.1016/j.actamat.2016.02.014.
- [26] S.A. Khairallah, A. Anderson, Mesoscopic simulation model of selective laser melting of stainless steel powder, *J. Mater. Process. Technol.* 214 (2014) 2627–2636.
- [27] A. Gusarov, I. Smurov, Modeling the interaction of laser radiation with powder bed at selective laser melting, *Phys. Procedia*. 5 (2010) 381–394.
- [28] T. Vilaro, C. Colin, J.D. Bartout, As-Fabricated and Heat-Treated Microstructures of the Ti-6Al-4V Alloy Processed by Selective Laser Melting, *Metall. Mater. Trans. A*. 42 (2011) 3190–3199. doi:10.1007/s11661-011-0731-y.
- [29] W.W. Duley, *Laser Welding*, Wiley, 1998. <https://books.google.ca/books?id=y916QgAACAAJ>.
- [30] C. Panwisawas, C.L. Qiu, Y. Sovani, J.W. Brooks, M.M. Attallah, H.C. Basoalto, On the role of thermal fluid dynamics into the evolution of porosity during selective laser melting, *Scr. Mater.* 105 (2015) 14–17. doi:10.1016/j.scriptamat.2015.04.016.
- [31] A. Kaplan, Metallurgy and Imperfections of Welding and Hardening, in: J. Dowden, W. Schulz (Eds.), *Theory Laser Mater. Process. Heat Mass Transf. Mod. Technol.*, Springer International Publishing, Cham, 2017: pp. 241–261. doi:10.1007/978-3-319-56711-2\_8.
- [32] H. Nakamura, Y. Kawahito, K. Nishimoto, S. Katayama, Elucidation of melt flows and spatter formation mechanisms during high power laser welding of pure titanium, *J. Laser Appl.* 27 (2015) 032012. doi:10.2351/1.4922383.
- [33] S.A. Khairallah, A.T. Anderson, A. Rubenchik, W.E. King, Laser powder-bed fusion additive manufacturing: Physics of complex melt flow and formation mechanisms of pores, spatter, and denudation zones, *Acta Mater.* 108 (2016) 36–45. doi:10.1016/j.actamat.2016.02.014.
- [34] X. Zhou, D. Wang, X. Liu, D. Zhang, S. Qu, J. Ma, G. London, Z. Shen, W. Liu, 3D-imaging of selective laser melting defects in a Co–Cr–Mo alloy by synchrotron radiation micro-CT, *Acta Mater.* 98 (2015) 1–16. doi:10.1016/j.actamat.2015.07.014.
- [35] S.M.H. Hojjatzadeh, N.D. Parab, W. Yan, Q. Guo, L. Xiong, C. Zhao, M. Qu, L.I. Escano, X. Xiao, K. Fezzaa, W. Everhart, T. Sun, L. Chen, Pore elimination mechanisms during 3D printing of metals, *Nat. Commun.* 10 (2019) 1–8. doi:10.1038/s41467-019-10973-9.